PNAS Nexus, 2023, 2, 1–10
https://doi.org/10.1093/pnasnexus/pgad250
Advance access publication 1 August 2023
Research Report

Short-wave infrared fluorescence imaging of near-infrared dyes with robust end-tail emission using a small-animal imaging device

Francesca Arena[a,*,1], Francesca La Cava[a,1], Daniele Faletto[a], Miriam Roberto[b], Federico Crivellin[a], Francesco Stummo[a], Alessia Adamo[a], Mariangela Boccalon[a], Roberta Napolitano[a], Francesco Blasi[a], Maximilian Koch[c], Adrian Taruttis[c] and Erika Reitano[c]

[a]Bracco Research Center, Bracco Imaging S.p.A., Turin 10010, Italy
[b]Molecular Imaging Center, Department of Molecular Biotechnologies and Health Sciences, University of Torino, Turin 10126, Italy
[c]SurgVision GmbH, Munich 81379, Germany
*To whom correspondence should be addressed: Email: francesca.arena@bracco.com
[1]F.A. and F.L.C. contributed equally to this work.
Edited By: Rui Reis

Abstract

Commercially available near-infrared (NIR) dyes, including indocyanine green (ICG), display an end-tail of the fluorescence emission spectrum detectable in the short-wave infrared (SWIR) window. Imaging methods based on the second NIR spectral region (1,000–1,700 nm) are gaining interest within the biomedical imaging community due to minimal autofluorescence and scattering, allowing higher spatial resolution and depth sensitivity. Using a SWIR fluorescence imaging device, the properties of ICG vs. heptamethine cyanine dyes with emission >800 nm were evaluated using tissue-simulating phantoms and animal experiments. In this study, we tested the hypothesis that an increased rigidity of the heptamethine chain may increase the SWIR imaging performance due to the bathochromic shift of the emission spectrum. Fluorescence SWIR imaging of capillary plastic tubes filled with dyes was followed by experiments on healthy animals in which a time series of fluorescence hindlimb images were analyzed. Our findings suggest that higher spatial resolution can be achieved even at greater depths (>5 mm) or longer wavelengths (>1,100 nm), in both tissue phantoms and animals, opening the possibility to translate the SWIR prototype toward clinical application.

Keywords: short-wave infrared imaging, hindlimb vasculature, deep-tissue imaging, principal component analysis, biomedical imaging

Significance Statement

The meaningfully reduced photon absorption, low tissue autofluorescence, and scattering in the short-wave infrared (SWIR) region (900–1,700 nm) opens many exciting ways for investigation of in vivo biological processes. By adding stiffness to the structures of the cyanine polymethine chain, it is possible to obtain stable dyes with a broad emission spectrum in the SWIR region. In this way, fluorophores that were designed for NIR applications can become very useful in SWIR imaging, accelerating clinical translation of this technology.

Introduction

The short-wave infrared (SWIR) window (900–1,700 nm), also defined as the second near-infrared (NIR) spectral region, is gaining interest within the biomedical imaging community due to the reduced photon absorption, low tissue autofluorescence and scattering, and wavelength-dependent absorption, allowing higher spatial resolution and depth sensitivity (1, 2). Such properties are driving biologists and imaging scientists to test SWIR fluorescence in preclinical and clinical settings (3–5). SWIR imaging devices require sensitive indium gallium arsenide (InGaAs)-based diode array detectors to minimize the scattering effect, coupled to an adequate 2D camera and a SWIR light source (e.g. temperature stabilized LEDs) to achieve greater tissue transparency compared with the NIR (700–900 nm) range. Using such system configurations, several groups have shown the ability of SWIR imaging to assess the microvasculature in small animals, improving upon and/or complementing conventional high-energy imaging modalities (6–8).

As for NIR fluorescence, the efficient combination of a SWIR device and a dye is a requirement to achieve high imaging

Competing Interest: The authors declare: F.A., F.L.C., D.F., F.C., F.S., A.A., M.B.,R.N., F.B. and E.R. are Bracco Imaging SpA employees. M.K. and A.T. are SurgVision GmbH employees. M.R. received a PhD fellowship from University of Torino.
Received: February 27, 2023. **Revised:** June 7, 2023. **Accepted:** July 25, 2023

performance. However, the clinical adoption of SWIR imaging is still hampered by the low availability of dyes with robust emission in the infrared region of the electromagnetic spectrum and biological properties that allow safe human dosing. Recently, it was observed that commercially available NIR dyes, including indocyanine green (ICG) and IRDye 800CW, display an end-tail of the fluorescence emission spectrum detectable in the SWIR window upon excitation at maximum absorbance (9, 10). Also, IR-820, a commercial NIR dye that differs from ICG in the presence of a chloro-cyclohexenyl ring in the center of the polymethine chain, has shown potential for SWIR fluorescence imaging due to an emission spectrum more shifted toward the infrared compared with ICG (11). Since the polymethine chain rigidity may affect both the emission spectrum and the stability of the dye (12), structural modifications to the polymethine chain may yield stable dyes with a broad emission spectrum in the SWIR region.

Herein, we performed a systematic investigation of the photophysical mechanisms of tail emission of the NIR dyes ICG, IR820, S2180, and S2493 to assess the structural determinants that may impact the SWIR imaging properties. Using a SWIR imaging system, optimized for end-tail imaging of ICG, the properties of each dye were examined using tissue-simulating phantoms and healthy mice experiments. The data reveal the structure–activity relationship of the NIR dyes tested for SWIR applications and remark the relevance of thorough characterization of dye–device compatibility and performance particularly for end-tail SWIR imaging to ensure high image fidelity.

Materials and methods

The materials and methods used in this study are described in detail in Materials and Methods S1. Information includes descriptions SWIR fluorescence imaging device and NIR fluorescence dyes used in this study, phantom imaging, SWIR fluorescence imaging in healthy mice, and dynamic contrast enhancement images. All the procedures involving animals were performed in accordance with the national and international laws on the use of experimental animals (L.D. 26/2014; Directives 2010/63/EU) under the Ministerial Authorization (project Research Number 867/2020-PR).

Results

Optical characterization of dyes

Four heptamethine cyanines (Fig. 1) have been characterized in terms of absorption and emission in SWIR range in water, methanol, and Seronorm (Table 1). ICG has the absorption peak around 800 nm and the emission peak around 820 nm with a long wavelength emission tail, which extends past the NIR region, according to its optical properties reported in several papers (13–15). Compared with ICG, IR-820 and S2180 are heptamethine dyes with a rigid chloro-cyclohexenyl ring in the center of the polymethine chain. Their absorption and emission wavelengths are shifted by about 30–35 nm compared with ICG. The bathochromic shift observed between rigidified vs. nonrigidified dyes is known (16) and exhibits the effect of the structural modification, which promotes a resonance increase and therefore absorption at longer wavelengths. Moreover, S2180 differs from IR820 by the presence of a sulfonate group on benzoindolic moieties. This structural modification does not affect the optical characteristics of the dye that maintains maximum absorption and emission wavelengths in each examined solvent similar to IR-820.

Compared with S2180, S2493 contains a chloro-cyclopentenyl ring in the center of the polymethine chain instead of chloro-cyclohexenyl. Despite it is commercially available, its optical properties and its applicability have not been studied so far. This further rigidification causes a bathochromic shift of 25–30 nm in maxima of absorption and emission compared with S2180 in each examined solvent.

Fluorescence emissions in the SWIR range were obtained with 780-nm Long-Pass (LP) filters, recording data from 1,000 to 1,400 nm and using the maximum absorption wavelength (λ_{max}, Abs) as excitation wavelength. All modifications of ICG structure lead to a higher fluorescence signal in SWIR region because the emissions are more shifted toward 900 nm. In particular, in Seronorm, IR-820 exhibited a higher fluorescent emission compared with ICG, S2180, and S2493 in the 1,100- to 1,200-nm wavelength window. To anticipate the results to be expected using the SWIR imaging device, the optical properties of the dyes were evaluated using fixed excitation (808 nm) and emission collection (1,100–1,300) settings (Fig. 2). All fluorophores under investigation produced measurable fluorescence in the SWIR window; however, the end-tail signal registered represented only a very small portion of the total emission spectrum.

The photostability of ICG, IR-820, S2180, and S2493 was investigated in phosphate buffered saline (PBS) solution under irradiation of lamp. After 60 min, the fluorescence intensity decreased by ~50% for S2493 and ~25% for ICG and S2180 but only ~9% for IR-820 (Fig. 2e).

Serum phantom imaging

Qualitative analysis of the dye dilutions in serum for ICG, IR820, S2180, and S2493 was represented in Fig. 3. In the graph, mean fluorescence intensity values of all dyes as a function of concentration were reported with linear fit of the data. SWIR fluorescent signal from all dyes was detectable in the imaging system with 1,100-nm LP filter over a large range of concentrations (0.1–0.001 μM). According to the optical properties of dyes, at 1,100 nm, both IR-820 and ICG showed the highest efficiency, followed by S2180 and S2493, respectively (Table 2). Given the use of a control sample with only serum, ICG showed the expected lowest limit of detection in SWIR imaging system to be 5 nM, followed by IR-820 and S2180, both with 10 nM, and by S2493 with the highest limit of detection (50 nM).

Intralipid phantom validation

Imaging acquisition with Intralipid phantom was performed to evaluate the image quality of ICG, S2180, IR-820, and S2493 ranging from 1,100 LP to 1,300 LP filters at different depth. The phantom was used to mimic the optical characteristics of biological tissues in the SWIR window. Capillaries containing dyes in serum with an outer diameter (OD) of 1.27 mm and inner diameter (ID) of 0.86 mm were irradiated in the SWIR device, and emission images were acquired by Goldeye G-032 camera at different depths with different filters (1,100-nm LP, 1,200-nm LP, and 1,300-nm LP) using exposure time of 20, 70, and 100 ms depending on the applied filter. Figure 4 shows the spatial resolution of the optical systems measured via full-width half maximum (FWHM) analysis, whose results for all dyes capillaries images at different depths are summarized in Table 3. The FWHM values of Intralipid immersed capillary tubes, with 1100 LP filter at 1- to 5-mm depth, were 0.92–4.04 mm, which is higher than those obtained with the 1,200 (0.81–2.82) and 1,300 LP filters (0.82–2.87). The effect of light scattering becomes stronger as depth increases with 1,100-nm LP

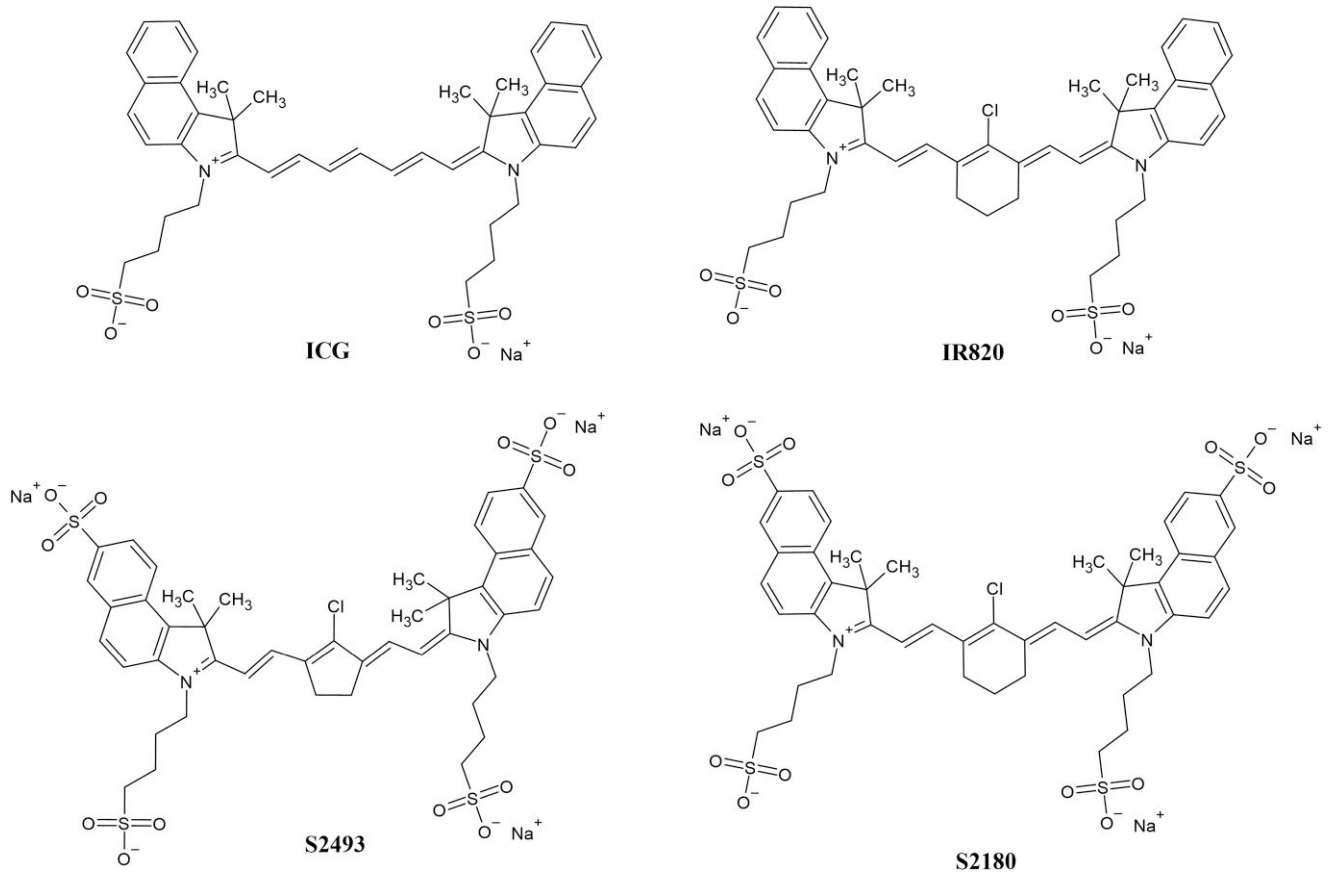

Fig. 1. Chemical structures of heptamethine cyanine.

Table 1. Optical properties of dyes.

Dye	Solvent	λ_{max}, Abs (nm)	λ_{max}, Em (nm)	AUC normalized intensity (1,000–1,400 nm)[a]
ICG	Water	780	805	2.4E6
	Methanol	785	815	11.3E6
	Seronorm	805	825	10.2E6
S2180	Water	815	835	3.8E6
	Methanol	823	842	15.8E6
	Seronorm	840	850	11.6E6
IR820	Water	812	830	1.7E6
	Methanol	820	843	9.5E6
	Seronorm	840	857	16.3E6
S2493	Water	840	860	5.7E6
	Methanol	850	870	19.0E6
	Seronorm	855	875	13.3E6

[a]Integral value of the emission tail between 1,000 and 1,400 nm using the maximum absorption wavelength (λ_{max}, Abs) of the dyes as excitation wavelength.

filter, while shape margins of the capillaries were more retained with both 1,200- and 1,300-nm LP filters, even at 3- and 5-mm depth. Considering the highest limit of detection observed in serum with S2493, a failure to visualize the lower depth capillary with the 1,300 LP filter was expected.

In vivo SWIR fluorescence imaging

The imaging performances of the dyes were tested by noninvasive in vivo imaging high-resolution system (Figs. S1 and S2) in mice ($n = 3$, for each dye). A 100-μL solution of ICG (1.0 mg/kg corresponding to 30 nmol/mouse), S2180 (1.2 mg/kg or 30 nmol/mouse), IR-820 (1.0 mg/kg or 30 nmol/mouse,) or S2493 (0.5 mg/kg corresponding to 10 nmol/mouse) was injected into mice via the tail vein catheter. The bolus injection of the dyes was followed by a 100-μL saline flush and the procedure not taking more than 5 s. The injected dose of S2493 used during the imaging experiment was reduced to 10 nmol/mouse, one-third of the dose taken with other dyes, as a result of aggregate formation when formulated using the same concentration of other dyes. An intense fluorescence signal was detected within few seconds after the injection under an excitation of 808 nm, and the whole hindlimb vascular system was clearly visualized within 5 min after the administration (Figs. 5 and S3). These images showed how dyes distributed throughout larger vessels into smaller ones. In particular, ICG, IR-820, and S2180 exhibited a clear visualization of the deep vasculature with high signal-to-noise contrast and high imaging resolution; S2493 produced a lower contrast in the vessels, likely due to the lower administration dose. In terms of blood persistence, S2180 and S2493 were both visible in the hindlimb vasculature up to 2 h after the administration, with an average half-life of ~34 and 55 min, respectively. On the contrary, ICG and IR-820 remain in the bloodstream for less than half an hour, thus reducing the possibility of seeing them in the vasculature until the last time points of the experiment. In particular for ICG, the interaction with serum protein was less evident and the possible photobleaching after long-time laser irradiation was observed.

The corresponding maximum feature widths calculated via the Gaussian fitted FWHM along the red line depicted in Fig. 5a on saphenous artery were 0.37, 0.34, and 0.30 mm for ICG, IR-820, and S2180, respectively, thus suggesting the high imaging resolution

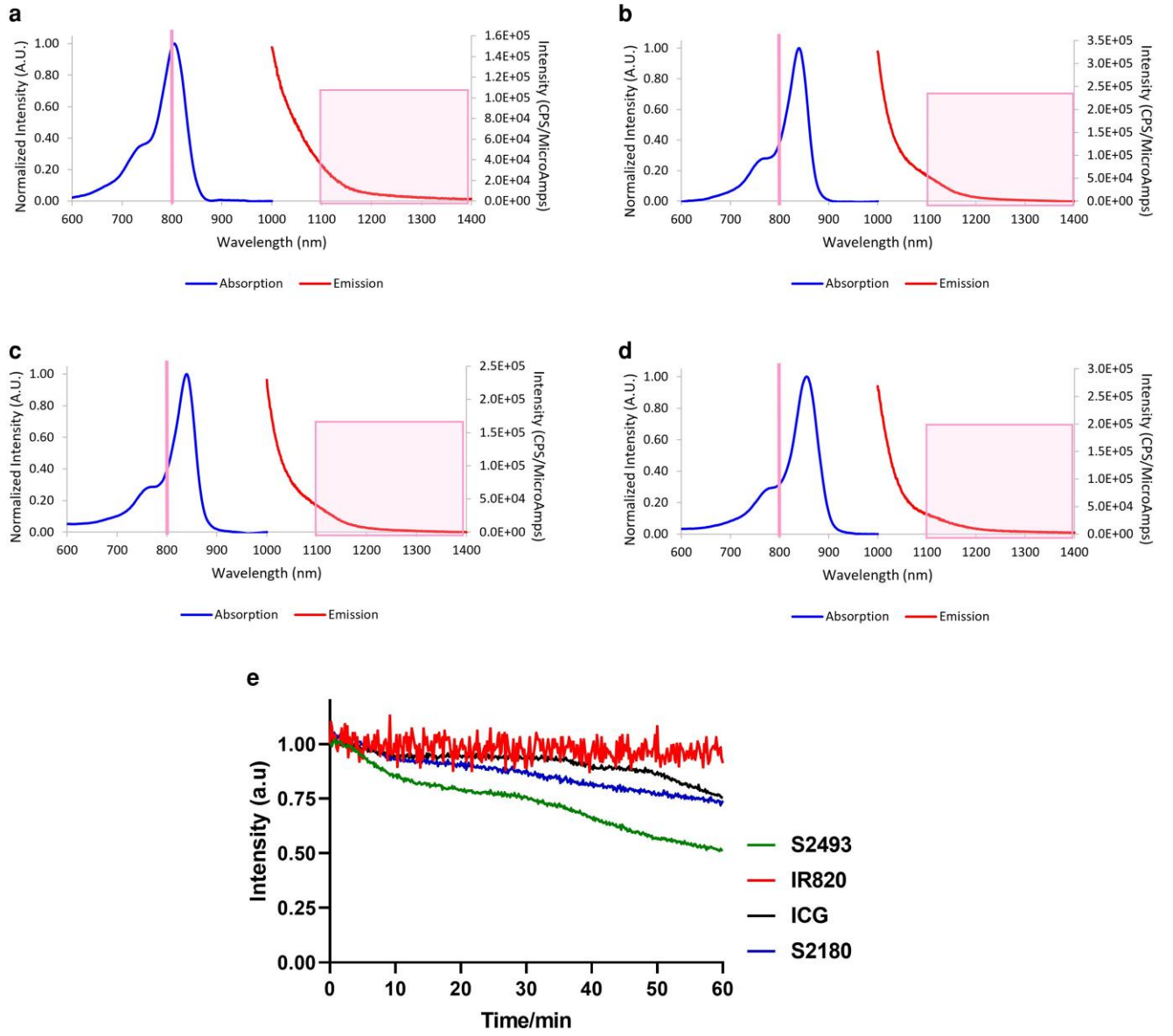

Fig. 2. Normalized absorption spectra with overlays indicating excitation SWIR wavelength (808 nm) and emission tail beyond 1,100 nm of a) ICG, b) IR820, c) S2180, and d) S2493. e) Normalized fluorescence intensity of dyes solution in PBS illuminated with lamp for 60 min.

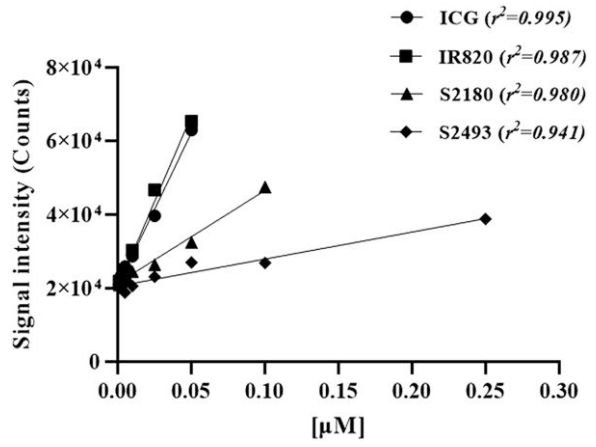

Fig. 3. Fluorescence intensities of phantom images as a function of dyes concentration with linear fits and Pearson's coefficients.

Table 2. Fluorescent detectable level of dyes.

Dye	LOD/(μM)	LOQ/(μM)
ICG	0.005	0.025
S2493	0.05	0.25
S2180	0.01	0.05
IR820	0.01	0.025

performances of these dyes (Fig. 6). S2493 showed a lower imaging resolution defining a maximum feature width of 0.6 mm. The minimal tissue autofluorescence, low absorption, and scattering in the SWIR region allowed also reliable imaging of deeper vessels such as epigastric artery (blue line in Fig. 5a). High-order branches of blood vessels were well defined with high spatial resolution, and a diameter of about 0.23 mm could be unambiguously identified with all dyes but S2493 (about 0.5 mm). As reported in Fig. 6, the corresponding

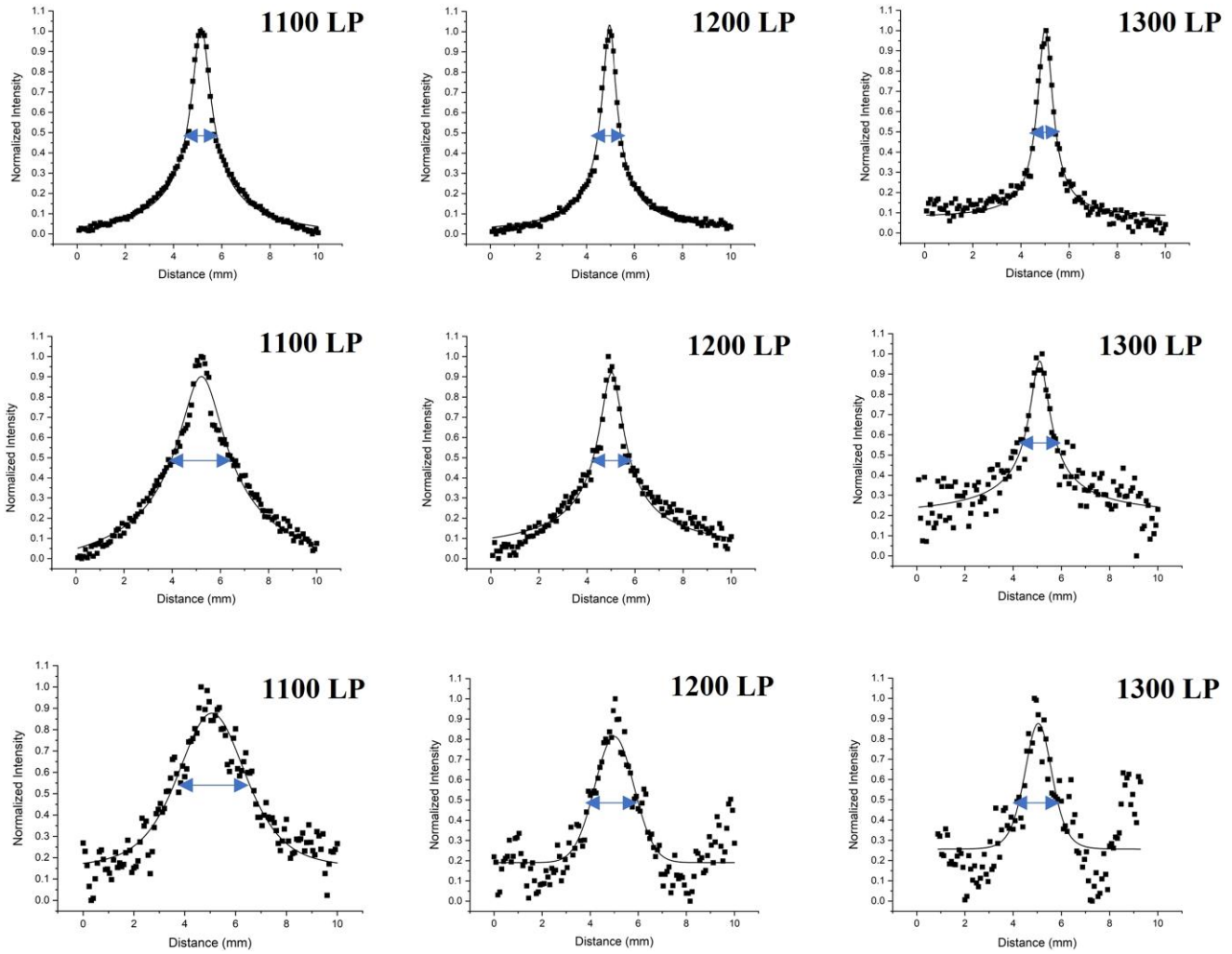

Fig. 4. Intralipid® phantom study of ICG, IR-820, S2180, and S2493. Fluorescence intensity signal (square dots) and Gaussian fitting curve (solid line) along capillary at a) 1, b) 3, and c) 5 mm from the Intralipid® surface acquired with various filters (1,100-nm LP, 1,200-nm LP, and 1,300-nm LP).

feature resolutions obtained with ICG, IR820, and S2180 in smaller hindlimb vasculature displayed calculated vessel diameter values consistent with expected values (represented in the graph with dotted line and reported in the literature (17)), suggesting high imaging resolution performances of dyes. The diameter resolution obtained with S2493 in the smaller hindlimb vasculature was a little far from the anticipated value, as already observed in the principal vasculature. Noticeably, even the epigastric artery can be clearly seen in supine position, indicating a penetration depth of >5 mm for SWIR imaging system.

The discrimination of vessels with a smaller diameter was significantly improved at longer wavelengths. Mice intravenously injected with 0.1-mL IR820 buffered solution (1.0 mg/kg) were acquired with both 1,100-nm LP and 1,200-nm LP filters to evaluate the light scattering effect in the different SWIR spectral regions. Mouse hindlimb vasculature was clearly visualized in both SWIR images, with different spatial resolutions (Fig. 7a). Figure 7b shows the FWHM Gaussian measurement of the epigastric artery (marked in blue). FWHM values of vessels were 0.24 (1,100-nm LP filter) and 0.10 mm (1,200-nm LP filter), respectively.

Besides results on vasculature, biodistribution evaluation was also performed, because biocompatibility and high excretion rates are important features for dyes and imaging agents to be used in biological studies and clinical applications. Ex vivo imaging of harvested organs (spleen, intestine, liver, kidney, and muscle considered as background tissue) 24 h after intravenous injection of the dyes revealed predominant liver uptake for IR-820 compared with S2180 and S2493, which showed mixed renal and hepatic accumulation (Fig. 8). In comparison with the other dyes, ICG showed very fast circulation with lower fluorescent signal distribution in the excretory organs at this late time point.

Vessel resolution through PCA

To obtain further physiological and anatomical information on the mouse vasculature, principal component analysis (PCA) was applied to a time series of fluorescence images in the first 100 s (200 frames) immediately after injection (Movie S1). The initial PCA component, which could be interpreted as the strongest temporal changes of the respective pixels, unveils fine structures that are not visible in any of the single frames throughout the video (Fig. 9). It can be noted that the different temporal responses of pixels throughout the entire video depict the vessels attribution between arteries and veins in a single image.

The resulting image has notable correspondence with an anatomical laboratory atlas (18) and demonstrates the remarkable spatial resolution obtained with the SWIR imaging device.

Table 3. FWHM values of capillaries filled with dyes in serum at different depth in Intralipid.

Dye	FWHM (mm)								
	1,100 LP	1,200 LP	1,300 LP	1,100 LP	1,200 LP	1,300 LP	1,100 LP	1,200 LP	1,300 LP
	1 mm			3 mm			5 mm		
ICG	1.28	0.91	0.82	3.33	1.69	1.34	3.16	1.87	1.33
S2493	1.08	0.87	0.85	4.04	2.48	1.22	2.44	1.79	—
S2180	0.92	0.81	0.91	3.20	1.77	1.42	2.59	1.80	2.87
IR820	1.20	0.94	0.87	4.01	2.82	1.20	2.75	1.75	1.88

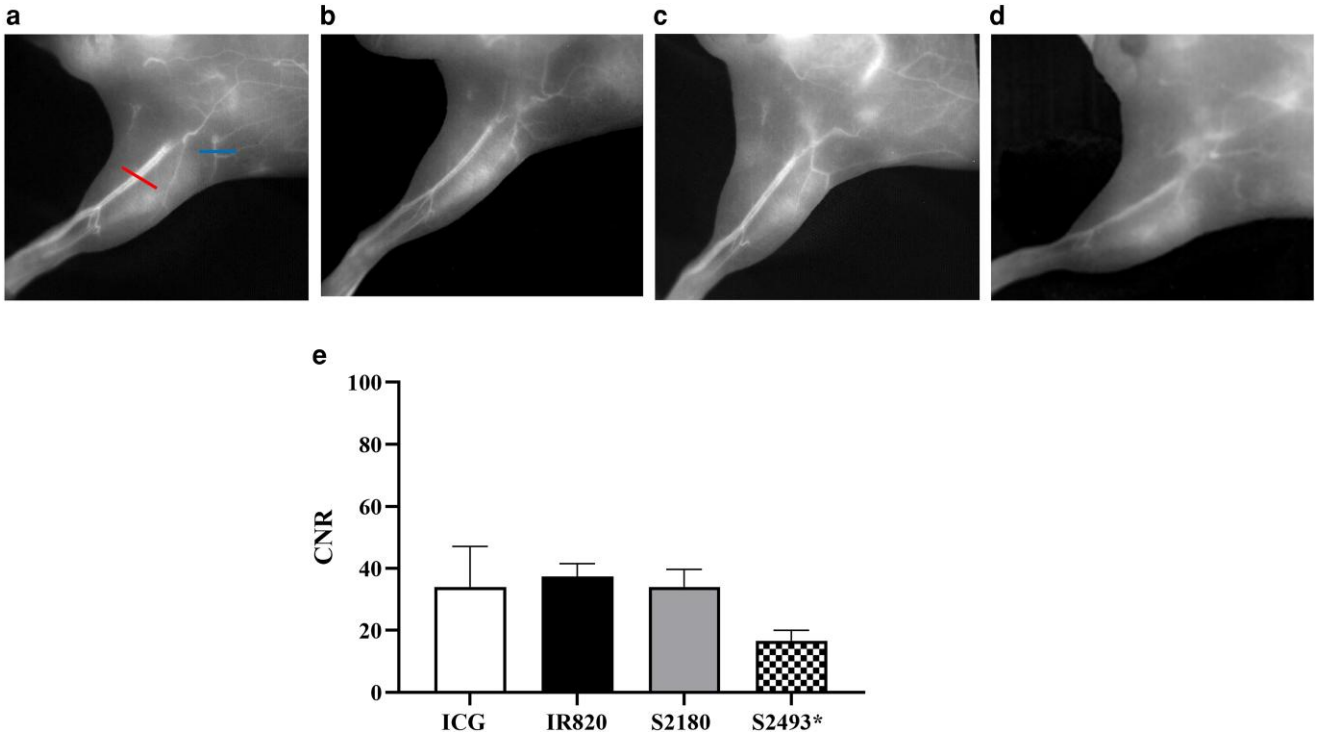

Fig. 5. In vivo imaging of mice hindlimb vasculature with ICG, IR820, S2180, and S2493. Fluorescence images of representative live mice 5 min after intravenous injection into tail vein of a) ICG, b) IR820, c) S2180, and d) S2493 (30 and 10 nmol/mouse, 100 µL. e) Contrast-to-noise ratio (CNR) in saphenous artery of animals injected with ICG, IR820, S2180, and S2493 5 min after ($n = 3$). Asterisks indicate that S2493 was administered at one-third of the dose of the other compounds.

Discussion

A self-built SWIR imaging system was developed and applied to small animals for detailed evaluation of the deep vasculature, using different NIR dyes. In addition to fast imaging speed and ease of use, the SWIR imaging system has shown the ability to image small blood vessels in vivo, exemplified by the visualization of hindlimb vessels in mice. The preclinical SWIR system also has demonstrated the advantage of obtaining high spatial resolution images, with the possibility of detecting high-order branches of blood vessels and blood flow in a noninvasive way. This system was optimized for SWIR ICG imaging because, first, ICG provides significant fluorescence emission in the SWIR wavelength range and, second, because ICG is already utilized in clinical practice and can therefore provide a shortened route to clinical translation of SWIR imaging. Clinical translation of the imaging system for investigational use is a topic of further research and development, with the main changes required being related to the form factor of the device; while the current system utilizes a light-tight chamber suitable for imaging small animals, an investigational clinical device requires an open form that can be used to image parts of the anatomy, for example during surgery. However, the primary components of the device, being the camera and excitation light sources, appear suitable for clinical scenarios because of their sufficiently compact size and achievable cooling requirements. Other SWIR fluorescence imaging systems have been reported in the literature, for example commercial small-animal laboratory devices (19, 20) and academic research device (2, 21). In contrast to many devices described in the literature, the SWIR imaging system does not use high-powered laser excitation or a deep-cooled camera, rather LED illumination, potentially easing device development and clinical translation.

In addition considering that hundreds of thousands of ICG-based NIR imaging procedures are performed each year in surgical robotics alone, adopting modifications of commercial NIR dyes to optimize the molecules for end-tail SWIR imaging and moving toward dual silicon/InGaAs endoscope sensors could directly improve the sensibility of cancer imaging.

The development of specific dyes for SWIR imaging is an ongoing effort, and several novel molecular entities having

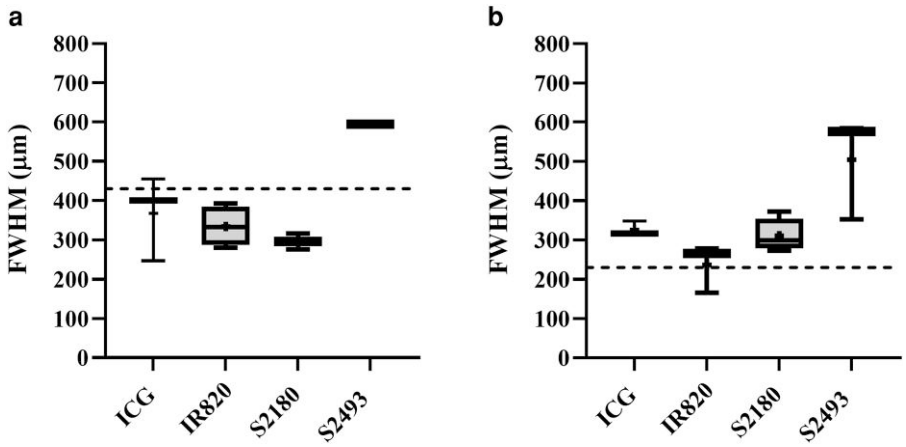

Fig. 6. FWHM of a) saphenous and b) epigastric artery measured in SWIR acquisitions after intravenous injection in $n = 3$ animals each with ICG, IR820, S2180, and S2493. Dotted line in graphs indicates the saphenous artery diameter (ca. 430 µm) and the epigastric artery diameter (ca. 230 µm) as detailed in literature (17).

maximum absorption and emission properties beyond 1,000 nm have been proposed in the past few years (22). In principle, such new dyes are superior for SWIR applications to conventional NIR fluorophores due to their native infrared spectrum. However, such molecules have often greater structural complexity than NIR dyes and may suffer from low brightness and solubility in aqueous media and low stability, further challenging product development and full translation. Moreover small organic fluorophores spectrally active in the 900- to 1,700-nm region work well as micelles or nanomaterials that raise concerns in terms of their retention and accumulation due to the potential immunogenic response. The strategy of repurposing NIR dyes for SWIR imaging, currently explored by several groups (23), may offer some advantages compared with the abovementioned build-from-scratch option. Clinical translation and adoption of SWIR imaging technologies may be accelerated by repurposing NIR dyes since ICG is already widely used in clinical practice for intraoperative applications, and the clinical development of new NIR probes for molecular fluorescence-guided surgery is progressing with high momentum, as highlighted by the recent approval of Cytalux (Pafolacianine Sodium, On Target Laboratories) by the Food and Drug Administration for ovarian cancer surgery (24). Structural modifications of commercial NIR dyes may be implemented to optimize the molecules for end-tail SWIR imaging. However, for this application, the structure–activity relationship of the NIR dyes is not obvious or well defined; thus, several attributes need to be balanced and experimentally tested to derive an optimal dye for end-tail SWIR imaging. In this study, we tested the hypothesis that an increased rigidity of the heptamethine chain may increase the SWIR imaging performance due to the bathochromic shift of the emission spectrum. We found that a bathochromic shift up to 70 nm can be obtained by increasing the rigidity of the cyanine dyes, which, for some molecules, yielded about two to three times increase of SWIR emission, expressed as $AUC_{1,000–1,400\,nm}$, compared with the reference ICG. Nonetheless, the sole shift was not sufficient to significantly boost the SWIR end-tail emission of the molecules, since the emission peak is still too far from the SWIR detection region.

Phantom studies using the preclinical SWIR device displayed that fluorescence was readily detectable for all tested NIR dyes, showing a robust linear response to the lowest concentration imaged (up to 10 nM). Although ICG presented the lowest limit of detection, due to the abovementioned design features of the device, all dyes could be detected in the nanomolar concentration range, supporting potential applications beyond vascular perfusion imaging, which was the focus of the present work. The Intralipid phantoms described in this study were chosen to investigate the effect of an absorbing and scattering agent (Intralipid) on the dyes in the SWIR window. It is well known that Intralipid has scattering properties similar to the skin (25) in which the dissemination behavior decreases with increasing wavelength (3). All dyes acquired in Intralipid phantoms lose some image information already at 3 mm of depth when imaged with 1,100-nm LP filter. By changing the wavelength in SWIR window (1,200 LP and 1,300 LP ranges), the lower albedo leads to better maintenance of the feature information and visualization of the correct FWHM value of capillaries also at 5 mm of depth.

These abovementioned good performances obtained with the SWIR preclinical device have also been confirmed with the visualization of dyes in the hindlimb blood vessel networks.

ICG, S2180, and IR-820 were clearly visualized right after the administration with high magnification in the hindlimb vasculature under the SWIR preclinical device. Interestingly, S2493, which was administered at one-third of the dose, showed reliable contrast in vessels, demonstrating a performance comparable with that of the other dyes. Compared with in vivo published studies with fluorescent semiconducting polymer dots (26), single-wallet carbon nanotubes (SWNTs), and/or the organic dye FD-1080 (6, 27), our SWIR preclinical device achieved a hindlimb vessel resolution lower than 0.2 mm with tested dyes. Furthermore, the deeper abdominal vessels including the inferior epigastric could be clearly imaged using both 1,100-nm LP and 1,200-nm LP filters. The reduced autofluorescence and photon scattering of tissues at 1,200 nm allowed a qualitative superior image contrast of the hindlimb vessels, especially with IR-820 compared with ICG.

It should also be noted that dyes showed a different behavior after administration in mice. IR-820 remained more in circulation, as well as S2180 and S2493, compared with ICG. This could be ascribed to greater interaction with serum proteins that may increase also their serum stability.

In an attempt to obtain also additional anatomical information, PCA was applied to the time series of hindlimb fluorescence images of NIR dye in SWIR imaging. PCA is a common statistical processing method for compressing high-dimensional data into a lower-dimensional form by choosing only the highest variance

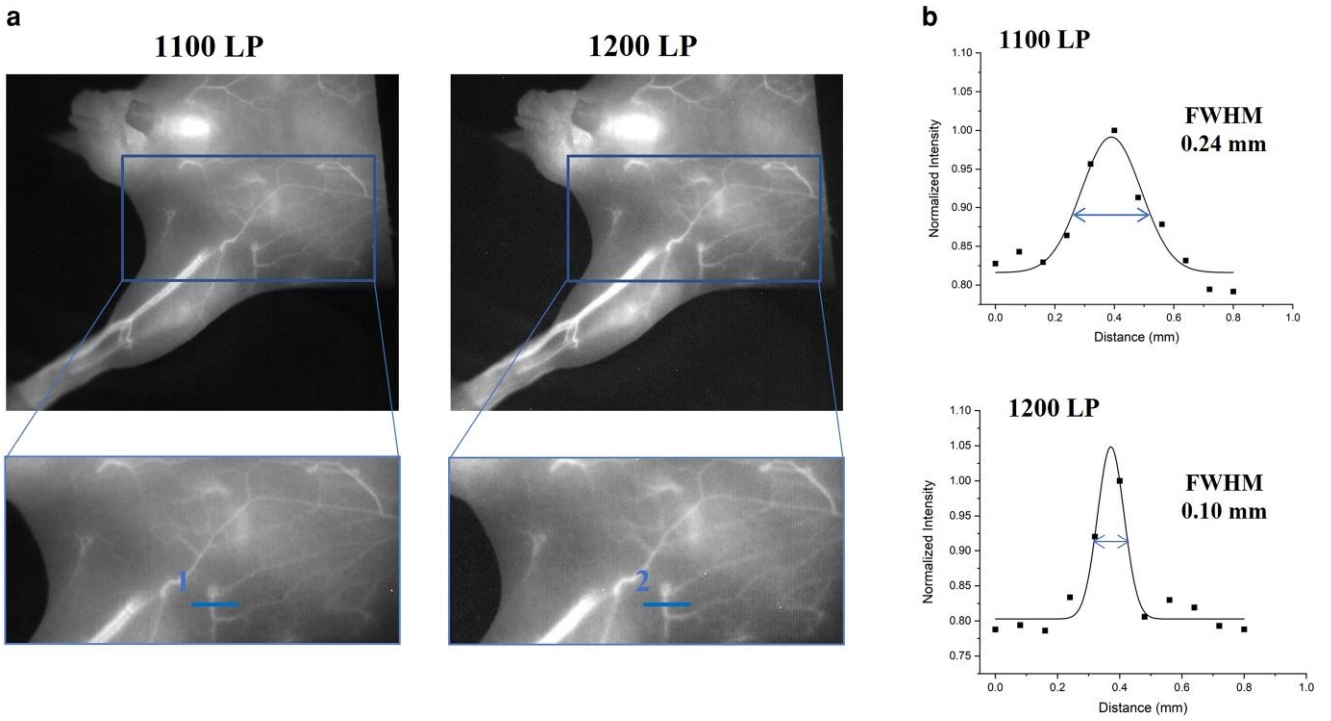

Fig. 7. a) SWIR imaging of mice hindlimb in supine position after intravenous injection of IR820 ($n = 3$) with different filters. b) Fluorescence intensity signals (square dots) and Gaussian fitting curve (solid line) along lines 1 and 2 in the SWIR images showed in a).

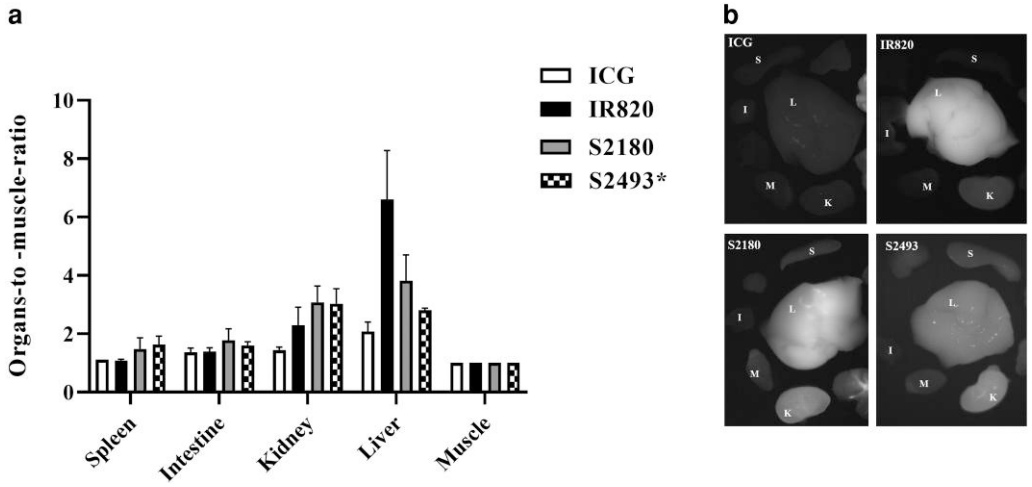

Fig. 8. Biodistribution of ICG, IR820, S2180, and S2493. a) Organ-to-muscle ratio obtained in SWIR acquisition of excised organs 24 h after administration of dyes. b) Visual distribution of signal intensity for major organs. I, intestine; K, kidney; L, liver; M, muscle; S, spleen. Asterisk indicates that S2493 was administered at one-third of the dose of the other compounds.

components of the data set, which is a powerful tool for analyzing time-related activity (28, 29). The determination of both arterial and venous vessels, anatomically and hemodynamically, was allowed by PCA analysis in the hindlimb compartment.

We acknowledge a few potential shortcomings of our study. Firstly, the excitation wavelength of the SWIR preclinical device was optimized by design for the spectrum of ICG in the blood, not corresponding to the absorption maxima of the other fluorophores tested. In fact, at 808 nm, the absorbance of S2180, IR-820, and S2493 is not at peak, rather 30–50% of the maxima. Such limitation did not impair the detection of low concentrations and high-quality imaging for the blood vessel for S2180, IR-820, and S2493; however, the suboptimal illumination did not allow to perform a fair comparison between the dyes. Another potential bias of the study, particularly related to the in vivo imaging properties of the dye, is the slight difference in formulation composition and dosing between fluorophores. Such slight differences may have only marginally impacted the overall conclusions of the study, since the in vivo analyses were mainly qualitative and/or ratiometric (e.g. tissue-to-background ratio). Relative to both points, an absolute quantitative comparison among the dyes using the SWIR preclinical device was not the aim of the study. Future studies will aim at addressing such shortcoming once a candidate dye will be selected and the SWIR device further optimizes as necessary to fully exploit its optical properties.

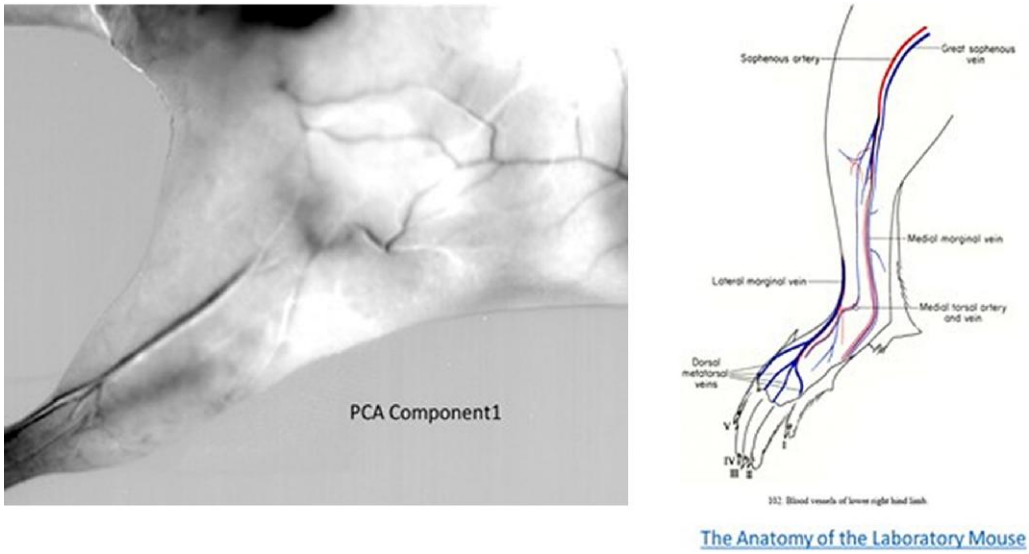

Fig. 9. In vivo imaging of mice hindlimb vasculature of mouse with PCA to distinguish arterial (dark) from venous (clear) vessels.

Conclusion

A self-built SWIR preclinical device was successfully tested by phantom studies and small-animal imaging experiments with commercially available dyes, including ICG, which is currently used for NIR fluorescence imaging. The high sensitivity and spatial resolution at depth provided by the SWIR device may warrant further development toward a clinical investigational prototype.

NIR dyes repurposing for SWIR imaging appear to be feasible in principle, due to their end-tail emission; however, it should be stressed that only a small portion of the emission spectrum of the dye is captured beyond 1,000 nm. Further investigation of the structure–activity relationship of the dyes and deep assessment of image fidelity using clinical SWIR devices are necessary to fully gauge on the potential of the technology for medical applications, in particular in comparison with the well-established use of NIR fluorescence imaging.

Supplementary material

Supplementary material is available at *PNAS Nexus* online.

Funding

The authors declare no funding.

Data availability

Access to experimental data is subjected to restrictions due to Company's confidentiality policy.

Author contributions

F.A., F.L.C., R.N., F.B., A.T., and E.R. designed the research; F.A., F.L.C., D.F., M.R., and E.R. performed the research; F.C., F.S., A.A., M.B., contributed the new product/analytic tools; F.A., F.L.C., D.F., M.R., and M.K. analyzed the data; and F.A., F.L.C., D.F., M.B., and M.K. wrote the paper.

References

1 Koch M, Ntziachristos V. 2016. Advancing surgical vision with fluorescence imaging. *Annu Rev Med*. 67:153–164.
2 Carr J-A, *et al.* 2018. Shortwave infrared fluorescence imaging with the clinically approved near-infrared dye indocyanine green. *Proc Natl Acad Sci U S A*. 115:4465–4470.
3 Welsher K, Sherlock S-P, Dai H. 2011. Deep-tissue anatomical imaging of mice using carbon nanotube fluorophores in the second near-infrared window. *Proc Natl Acad Sci U S A*. 108:8943–8948.
4 Shi L, Sordillo L-A, Rodríguez-Contreras A, Alfano R. 2016. Transmission in near-infrared optical windows for deep brain imaging. *J Biophotonics*. 9:38–43.
5 Li C, *et al.* 2022. NIR-II bioimaging of small molecule fluorophores: from basic research to clinical applications. *Biosens Bioelectron*. 216:114620.
6 Hong G, *et al.* 2012. Multifunctional in vivo vascular imaging using near-infrared II fluorescence. *Nat Med*. 18:1841–1846.
7 Li C, *et al.* 2014. In vivo real-time visualization of tissue blood flow and angiogenesis using Ag2S quantum dots in the NIR-II window. *Biomaterials* 35:393–400.
8 Hong G, *et al.* 2014. Near-infrared II fluorescence for imaging hindlimb vessel regeneration with dynamic tissue perfusion measurement. *Circ Cardiovasc Imaging*. 3:517–525.
9 Starosolski Z, *et al.* 2017. Indocyanine green fluorescence in second near-infrared (NIR-II) window. *PLoS One* 12:e0187563.
10 Zhu S, *et al.* 2018. Near-infrared-II (NIR-II) bioimaging via off-peak NIR-I fluorescence emission. *Theranostics* 8:4141–4151.
11 Feng Z, *et al.* 2019. Excretable IR-820 for in vivo NIR-II fluorescence cerebrovascular imaging and photothermal therapy of subcutaneous tumor. *Theranostics* 9:5706–5719.
12 Fernandez-Fernandez A, *et al.* 2012. Comparative study of the optical and heat generation properties of IR820 and indocyanine green. *Mol Imaging*. 11:99–113.
13 Philipa R, Penzkofera A, Bäumlerb W, Szeimiesb RM, Abels C. 1996. Absorption and fluorescence spectroscopic investigation of indocyanine green. *J Photochem Photobiol Chem*. 96: 137–148.

14 Saxena V, Sadoqi M, Shao J. 2003. Degradation kinetics of indocyanine green in aqueous solution. *J Pharm Sci*. 92:2090–2097.

15 Cosco ED, Lim I, Sletten EM. 2021. Photophysical properties of indocyanine green in the shortwave infrared region. *ChemPhotoChem*. 5:727–734.

16 Conceição DS, Ferreira DP, Ferreira LF. 2013. Photochemistry and cytotoxicity evaluation of heptamethinecyanine near infrared (NIR) dyes. *Int J Mol Sci*. 14:18557–18571.

17 Aslanidou L, *et al.* 2016. A 1D model of the arterial circulation in mice. *ALTEX*. 33:13–28.

18 Cook M-J. 1965. *The anatomy of the laboratory mouse*. New York: Academic Press.

19 Mateos S, *et al.* 2020. Instantaneous in vivo imaging of acute myocardial infarct by NIR-II luminescent nanodots. *Small* 16: 1907171.

20 Rodríguez-Luna M-R, *et al.* 2022. In vivo imaging evaluation of fluorescence intensity at tail emission of near-infrared-I (NIR-I) fluorophores in a porcine model. *Life (Basel)* 12:1123.

21 Wu D, *et al.* 2020. Extrahepatic cholangiography in near-infrared II window with the clinically approved fluorescence agent indocyanine green: a promising imaging technology for intraoperative diagnosis. *Theranostics* 10:3636–3651.

22 Yang Y, Zhang F. 2022. Molecular fluorophores for in vivo bioimaging in the second near-infrared window. *Eur J Nucl Med Mol Imaging*. 49:3226–3246.

23 Zhu S, *et al.* 2018. Repurposing cyanine NIR-I dyes accelerates clinical translation of near-infrared-II (NIR-II) bioimaging. *Adv Mater*. 9:1802546.

24 FDA news release. https://www.fda.gov/news-events/press-announcements/fda-approves-new-imaging-drug-help-identify-ovarian-cancer-lesions.

25 Samkoe K-S, *et al.* 2017. Development and evaluation of a connective tissue phantom model for subsurface visualization of cancers requiring wide local excision. *J Biomed Opt*. 22:1–12.

26 Li B, Lu L, Zhao M, Lei Z, Zhang F. 2018. An efficient 1064 nm NIR-II excitation fluorescent molecular dye for deep-tissue high-resolution dynamic bioimaging. *Angew. Chem. Int. Ed*. 57:7483–7487.

27 Su S-P, *et al.* 2022. Development of stereo NIR-II fluorescence imaging system for 3D tumor vasculature in small animals. *Biosensors (Basel)* 12:85.

28 Ringnér M. 2008. What is principal component analysis? *Nat Biotechnol*. 26:303–304.

29 Abdi H, Williams L-J. 2010. Principal component analysis. *Wiley Interdiscip Rev Comput Stat*. 2:433–459.